Chemical vapor deposition of titanium nitride thin films: kinetics and experiments

Juan Su, Rapahel Boichot, Elisabeth Blanquet, Frederic Mercier, Michel Pons

CrystEngComm, Royal Society of Chemistry, 2019, 21 (26), pp.3974-3981. ⟨10.1039/C9CE00488B⟩

Chemical vapor deposition of titanium nitride thin films: kinetics and experiments

Juan Su [1], Raphaël Boichot [1,*], Elisabeth Blanquet [1], Frédéric Mercier [1], and Michel Pons [1]

[1] Univ. Grenoble Alpes, CNRS, Grenoble INP*, SIMaP, F-38000 Grenoble, France. * Institute of Engineering Univ. Grenoble Alpes; juan.su@grenoble-inp.fr; elisabeth.blanquet@grenoble-inp.fr; frederic.mercier@grenoble-inp.fr; michel.pons@grenoble-inp.fr

* Correspondence: raphael.boichot@grenoble-inp.fr; Tel.: +33-476826537

Received: date; Accepted: date; Published: date

Abstract: Titanium nitride (TiN) films were grown by CVD (Chemical Vapor Deposition) from titanium chlorides generated *in situ* by direct chlorination of titanium metal, ammonia (NH_3) and hydrogen (H_2) as carrier gas on single crystal c-plane sapphire (Al_2O_3), cemented carbides (WC-Co), stainless steel (AFNOR Z150CDV12) and amorphous graphite substrates. Kinetic pathways involving four surface reactions has been proposed to simulate the growth rate. The proposed model has been validated by experiments performed at different temperatures (650-1400 °C), pressures (300-1000 Pa), with different amount of precursors (N/Ti ratio in gas phase) and on different substrates. The study shows that on polycrystalline materials, the crystal orientation depends on supersaturation while (111) preferred orientation is forced by underlying c-plane sapphire whatever the supersaturation. The low N/Ti ratio in gas phase leads to low growth rate and dense TiN film which is the key to obtain golden TiN. The high growth rate corresponds to brown TiN. Globally, the study shows that golden color is independent from texture and is just the natural aspect of a dense stoichiometric TiN layer.

Keywords: TiN; Chemical Vapor Deposition; Supersaturation; Decorative and functional coatings.

1. Introduction

Thin films of titanium nitride (TiN) have been widely applied as wear resistant coatings for tools [1-6], diffusion barrier layers [7-10], decorative layers [11,12] and for its high hardness, thermal and chemical stability and good electrical conductivity. Chemical Vapor Deposition (CVD) [13] is a common technique for the growth of TiN thin films [5,6,12,14-16]. Particularly, two major chemical systems for the thermal CVD of TiN coatings, $TiCl_4$–N_2–H_2 and $TiCl_4$–NH_3–H_2, are used [17]. The temperature range for the first system is 900–1200 °C due to the low reactivity of nitrogen [18]. The temperature range for the second system can be easily lowered to 550–750 °C [12]. The effects of process parameters on the growth rate of CVD TiN coatings have been studied by Kuo et al. [19] for the $TiCl_4$–N_2–H_2 system and by Jiang et al. [20] for the $TiCl_4$–NH_3–H_2 system. Due to the complexity of the process parameters, their experiments were only focused on process parameters such as partial pressure, temperature and the N/Ti ratio in gas phase. To the date, it is still difficult to predict which process conditions will lead to a certain texture or visual aspect in TiN due to discrepancies in the effect of parameters according to different authors and scattered data. In general, the growth rate is positively affected by increasing H_2, N_2, and NH_3 partial pressures but a positive to negative dependence of growth rate to increasing $TiCl_4$ partial pressure is observed in literature [17,21]. It results from the formation of a non-reactive complex, $TiCl_4NH_3$ in the gas phase. In this work, comprehensive link between supersaturation, temperature and growth rate will be presented combining experiments with CFD simulation.

A global kinetic model of TiN growth from $TiCl_4$-N_2-H_2 system was proposed in Ref. [17,21]. A detailed kinetic mechanism and reaction pathways were built for the $TiCl_4$-NH_3-H_2 system by Larson et al. and Allendorf et al. [22,23], but only for a temperature of 630°C. They estimated the growth rate by a series of surface reactions considering 4 gases, 10 surface sites and 2 bulk species. Grujicic et al. [24] applied this mechanism for multi-length scale modeling and showed that the grain size increased with increasing coating thickness. The thermodynamics and kinetics of gas-phase reactions in the Ti-Cl-H system was studied by Teyssandier et al. [25], the rate coefficients of decomposition of $TiCl_4$ and $TiCl_3$ [25] were confirmed by experiments at high temperature (1000-1200 °C) in Ref. [26]. The aim of this study is: (1) to assess simplified reaction pathways for the simulation of TiN growth with $TiCl_x$-NH_3-H_2 system based on the study of Larson and Allendorf [22] and extend it to a broad range of process temperature; (2) to improve the understanding of the relationships between growth rate, temperature, supersaturation, preferred orientation and morphology on ideal single crystal (c-plane sapphire) and polycrystalline materials (WC-Co, Stainless steel Z150CDV12, and amorphous graphite); (3) to figure out the main process parameters and the key feature for obtaining golden TiN.

2. Experimental details

TiN is grown on single crystal (0001) sapphire (The Roditi International corporation Ltd., London, UK), stainless steel (AFNOR Z150CDV12: 1.5%C, 12%Cr, 1%Mo and 1%V), WC-Co with 6 wt.% Cobalt (Hyperion, Grenoble, France) and amorphous graphite (Graphitech company, Saint Martin d'Hères, France). Due to the high hardness, WC-Co is first polished with diamond discs and finished by diamond suspension (1 μm). Stainless steel and graphite are finished with 1-μm (2400 grit) silicon carbide paper. These substrates are at the center of the graphite susceptor of 55 mm diameter. Deposition temperature is measured by a thermocouple (20-700 °C) or an infrared pyrometer (700-1400°C). The cold-wall experimental system used is shown in Figure 1. Ammonia NH_3 (99.999%) gas is injected from the side of the quartz tube to minimize gas-phase reactions before deposition. The others gases are injected from the top of reactor. Chlorine gas Cl_2 (99.999%) is injected into a chlorination tube which contains high purity titanium pellets (Goodfellow company, Coraopolis, PA, USA, purity of 99.98%). Lamps at the top of the quartz tube allow the chlorination reactions. Induction coils (20 kHz) are used to heat the graphite holder. The temperature of cooling water for the quartz tube is fixed at 85°C to minimize species condensation on walls. All the samples except graphite are cleaned by acetone, ethanol and isopropanol successively in an ultrasonic bath. Each cleaning procedure takes 5 minutes.

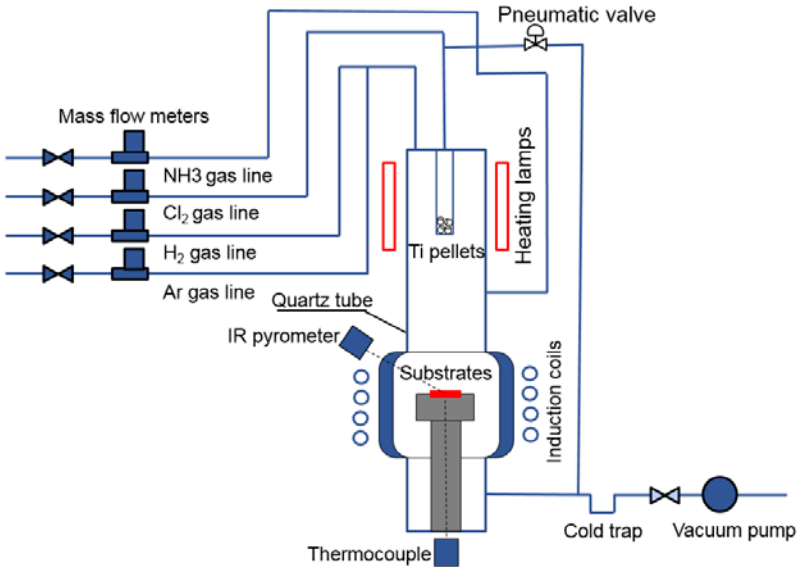

Figure 1. The cold wall experimental system for TiN CVD growth.

At the beginning of each run, 200 sccm of H_2 are injected into the chlorination tube to clean the titanium pellets at 650 °C for 20 minutes (removing of carbon contamination on the surface). The substrates are then heated under 1000 sccm of H_2 with a 30 K/min ramp to reach the working temperature, followed by a 10 min plateau (thermal stabilization). NH_3 is injected into the reactor 1 min before chlorine to reduce the etching of substrates by chlorides, especially when substrates are WC-Co (cobalt is particularly sensitive to chlorine). At the end of the experiment, the chlorine gas is switch off 1 min before NH_3. The H_2 flow is then replaced by 1000 sccm of N_2. The substrates are cooled down with a 37 K/min ramp.

In the present study, θ/2θ scans are made with a PANalytical X'Pert Pro MPD two-circle diffractometer (θ-θ, CuKα, acceleration voltage of 45 kV and current of 40 mA from a sealed x-ray tube) equipped with a 1D linear detector. Field Emission Gun-Scanning Electron Microscope (ZEISS Ultra-55) is used to characterize TiN layers surface morphology and texture. Thermodynamic analysis of the gas-phase chemistry is made using Factsage 7.2 thermodynamic software and the thermodynamic database FactPS. For the modeling of TiN deposition, heat transfer, mass transport and gas flow dynamics are solved using the CFD–ACE+ multiphysics software package (2017 version).

Table 1 summarized the experiments performed for this study. Experimental as well as modeling results are summarized in this table and will be discussed in next sections. To obtain the surface activation energy, the last 5 experiments in Table 1 are designed to vary the deposition temperature while the N/Ti ratio and pressure in the reactor are fixed at 1.5 and 1000 Pa, respectively. All the experiments in Table 1 are used to develop numerical modeling and simulation of TiN growth.

3. Modeling and simulation

3.1. Thermodynamic equilibrum and gas-phase kinetic analysis

For the traditional TiN coating system, $TiCl_4$ is generated by dosing and vaporizing its liquid phase. This solution necessitates handling liquid $TiCl_4$, a particularly corrosive product with a high vapor pressure. Teyssandier and Allendorf [25] have shown that $TiCl_4$ is stable and remains the most important Ti-containing species when the temperature is below 900 °C. In the chlorination system used here, Cl_2 gas passes over Ti pellets, solid $TiCl_2$ is theoretically the only chlorination product by thermodynamic calculation (large excess of titanium versus chlorine). This means that the titanium pellets are surrounded with solid $TiCl_2$ during chlorination process, that reacts in a second time with Cl_2. Figure 2 presents the thermodynamic equilibrium of 10 mol $TiCl_2$(s) and 2 mol Cl_2(g) at 1000 Pa in the 600-1000 °C temperature range, conditions close to our chlorination process. Some experiments are also carried out at around 300 Pa in this study, but the thermodynamic calculation shows that the total pressure does not affect the mole fraction of gaseous species. At 650 °C (chlorination temperature in the present work), the main gaseous species are $TiCl_3$(g) and $TiCl_4$(g) in equilibrium with solid-phase $TiCl_2$(s). Additionally, the deposition of a purple powdered films on the quartz tube is an indication of the presence of $TiCl_3$(g) (see Figure S1 in supplementary material). The mole fraction ratio is around $X_{TiCl3} : X_{TiCl4}=8 : 2$.

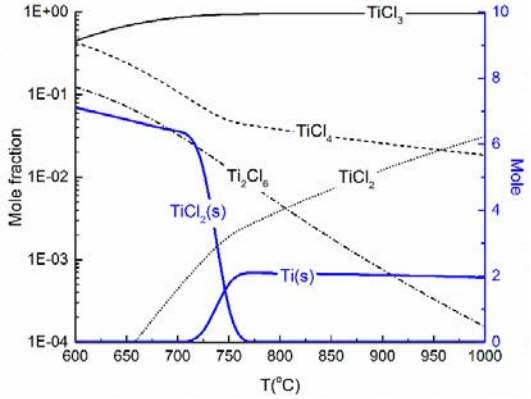

Figure 2. Mole fraction at equilibrium of a mixture of 2 mol Cl_2 (g) and 10 mol $TiCl_2$ (s) at 1000 Pa.

119 **Table 1.** Summary of the growth parameters. To calculate texture coefficient T_c, 4 main diffraction peaks are taken into account: (111), (200), (220) and (420).

Temperature °C	Pressure (Pa)	Sccm NH_3	Sccm Cl_2	N/Ti in gas phase	Measured growth rate (µm·h^{-1})	Theoretical growth rate (µm·h^{-1})	Log_{10} (surface supersaturation)	Main texture (T_c%) on c-plane sapphire	Main texture (T_c%) on WC-Co(*), graphite(#), steel(&)	Color on sapphire(*) and non-orientated substrates(#)
663	1000	25	20	1.875	1	2.9	13.4	111 (94%)	200* (100%)	brown*#
663	1000	50	20	3.75	7.7	5.7	13.63	111 (83%)	200* (100%)	brown*#
662	1000	50	10	7.5	5.7	5.64	13.57	111 (91%)	220* (93%)	brown*#
1100	1000	10	8	1.875	3	4.08	3.68	111 (100%)	-	golden*
710	310	5	7.5	1.0	0.06	0.228	11.39	111 (100%)	200* (100%)	silver*, golden#
673	310	5	5	1.5	0.04	0.2	12.39	111 (100%)	200* (100%)	silver*, golden#
665	1000	50	20	3.75	8.4	5.8	13.57	111 (73%)	200* (100%)	brown*#
604	1000	50	20	3.75	2.724	4.32	15.60	111 (57%), 200 (34%)	200* (100%)	brown*#

120 **Table 1.** Continued.

Temperature °C	Pressure (Pa)	Sccm NH_3	Sccm Cl_2	N/Ti in gas phase	Measured growth rate ($\mu m \cdot h^{-1}$)	Theoretical growth rate ($\mu m \cdot h^{-1}$)	Log_{10} (surface supersaturation)	Main texture (T_c%) on c-plane sapphire	Main texture (T_c%) on WC-Co(*), graphite(#), steel(&)	Color on sapphire(*) and non-orientated substrates(#)
609	1000	50	20	3.75	3	4.32	15.42	111 (86%)	200* (100%)	brown*#
619	1000	50	20	3.75	2.904	4.32	15.06	111 (93%)	200* (100%)	brown*#
662	1000	30	10	4.5	6.5	3.48	13.39	111 (100%)	200* (100%)	brown*#
662	1000	50	20	3.75	3.45	5.8	13.66	111(65%)	200* (100%)	brown*#
650	1000	5	5	1.5	0.3	0.58	13.0	-	200& (100%)	golden#
680	1000	5	5	1.5	0.4	0.6	12.16	-	200& (100%)	golden#
750	1000	5	5	1.5	0.6	0.84	10.21	-	200& (69%)	brown#
800	1000	5	5	1.5	0.7	1.02	8.96	-	200& (69%)	brown#
1400	1000	5	5	1.5	3.8	3.1	-0.135	111 (100%)	111# (62%)	Dark brown*#

121

For the traditional $TiCl_4$-NH_3 system, Umanskii et al. [27] studied the reaction pathways involving complex formation ($TiCl_xNH_y$). It was concluded that, in typical CVD conditions, only $TiCl_4NH_3$ is formed in substantial amount at low temperature. Grujicic et al. [24] took into account the presence of non-reactive complex formation. As $TiCl_4$(g) concentration is increased, it causes additional NH_3(g) to be tied up in the complex. This complex could be either poorly reactive, either with a very low vapor pressure and condensing. This decreases the concentration of NH_3(g) available for the CVD of TiN and, in turn, decreases the deposition rate. The effect is a very small negative order of the TiN deposition rate with respect to the concentration of $TiCl_4$(g). Teyssandier and Allendorf [25] developed a gas-phase kinetic model which corresponds to our experimental range. This dataset involving decomposition and formation of $TiCl_x$ (x=1, 2, 3, 4), and equilibrium reactions is used to understand gas-phase transformations as a function of temperature and pressure (see Table S2 in supplementary material).

3.2. Mass transport modeling

For mass transport modeling, the models and software packages already used for AlN deposition are used [28]. The governing equations of multicomponent mass transport and heat transfer can be found in Table S1 in supplementary material. The species properties such as diffusion coefficients, mixtures viscosities and thermal conductivities are calculated using the Enskog theory [29]. Lennard-Jones parameters for gaseous species are computed according to the empirical method in Ref. [30]. The laminar incompressible momentum equation is used to solve the diffusion-convection problem since the Reynolds number in all experiments is less than 50. The mixture enthalpy is calculated by a polynomial relationship with temperature by JANAF formalism [31].

To simplify the surface reaction model and figure out which $TiCl_x$ can be, $TiCl_x$ mole fractions on the substrate as a function of temperature at 300 Pa and 1000 Pa considering the 17 gas-phase reactions of the Ti-Cl-H system (see Table S2 in supplementary material) has been calculated by CFD-ACE as shown in Figure 3. The typical inlet gas-phase mole fractions are 90% H_2, 8% $TiCl_3$ and 2% $TiCl_4$ since $X_{TiCl3} : X_{TiCl4}=8 : 2$ from thermodynamic equilibrium in chlorination tube. It can be seen that the mole fraction of $TiCl_2$ is increasing and the mole fraction of $TiCl_4$ is decreasing with temperature, regardless of pressure. This conclusion is in a good agreement with Ref. [25,32]. The mole fraction of $TiCl_3$ is however almost stable, indicating that the decomposition and formation of $TiCl_3$ are almost kinetically balanced. Figure 3 further illustrates that $TiCl_3$ and $TiCl_4$ only should be considered for surface reactions and $TiCl_2$ can be ignored, because the mole fraction of $TiCl_2$ is negligible in typical CVD conditions.

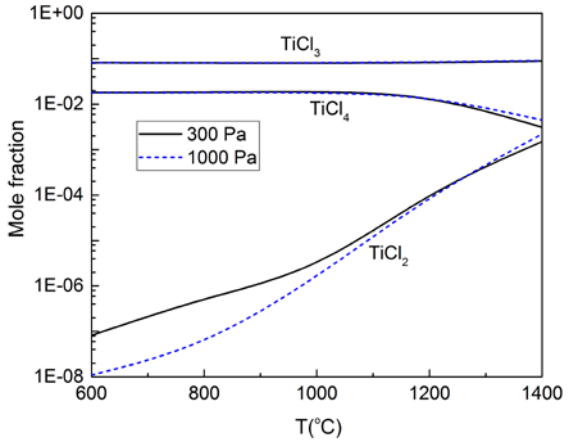

Figure 3. Mole fraction of $TiCl_x$ at the substrate center as a function of the deposition temperature.

The kinetic model of surface reactions developed by Allendorf et al. [23] was first used to compare experimental and modeling results at 630°C. This model involves 14 surface reactions and successfully predicts TiN growth rates as a function of key reactor parameters including inlet reactant concentrations, reactor pressures and total gas flow rates. This model will be modified to take into account the activation energy.

4. Results and discussion

4.1. Experimental growth rates versus modeling and the surface kinetic parameters

Arrhenius plot obtained at fixed flow rate and pressure (last five experiments in Table.1) is shown in Figure 4. It shows that the growth rate is kinetically controlled with an activation energy of 43 kJ/mol.

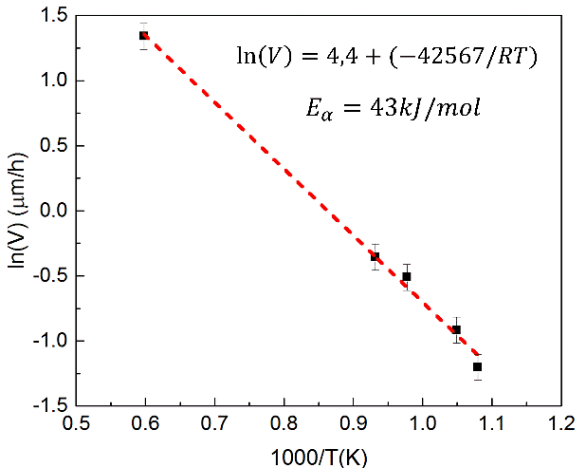

Figure 4. Arrhenius plots for TiN deposition.

From the previous kinetic database[23,25], a simplified kinetic model taking into account temperature variations is assumed.

$$TiCl_3 + NH_2\_s \rightarrow N(B) + TiCl_2\_s + HCl \quad (1)$$

$$TiCl_4 + NH_2\_s \rightarrow N(B) + TiCl_3\_s + HCl \quad (2)$$

$$NH_3 + TiCl_2\_s \rightarrow Ti(B) + NH_2\_s + HCl + Cl \quad (3)$$

$$NH_3 + TiCl_3\_s \rightarrow Ti(B) + NH_2\_s + HCl + Cl_2 \quad (4)$$

where three kinds of surface species on growing TiN surfaces are only considered: $TiCl_3\_s$, $TiCl_2\_s$ and NH_2_s. Surface reaction rate and kinetic data can be found in supplementary materials (see Table S3 in supplementary material).

Surface kinetic parameters have been obtained by minimizing the relative difference between experimental and simulated growth rates while maintaining kinetics from the original database [23] and varying the activation energy. It should be noted that each surface reaction conserves the total number of surface species, i.e. surface sites. In the case of the first reaction, for example, when a gas-species $TiCl_3$ attaches to the surface, there is one bulk phase atom added to the solid and a new surface species created. Reactions (1)-(4) are bimolecular reactions.

Although there are some reports of TiN deposition rates in the literature for $TiCl_4$-NH_3 system [21,23,33], the lack of detailed information makes it difficult to simulate the deposition rates published. The parity diagram between simulated and experimental growth rates from this work is presented in Figure 5. The experimental error originates from substrate temperature and thickness uncertainties.

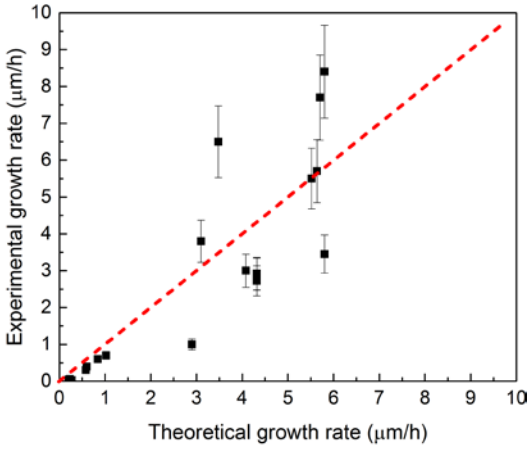

Figure 5. Parity diagram between experimental and theoretical growth rates from this work.

It is now possible to calculate the actual supersaturation (see equation S6 in supplementary materials for definition) just above the substrate by numerical modeling and to find relationships between processing parameters and microstructural information.

4.2. Relationship among the texture of TiN, growth rate and supersaturation

For each process conditions, the texture coefficient T_{c_hkl} for each (hkl) plane of the obtained film is calculated as follows [34],

$$T_{c\_hkl} = \frac{\frac{I_{hkl}}{I_{0,hkl}}}{\frac{1}{N} \cdot \sum_1^N \frac{I_{hkl}}{I_{0,hkl}}} \quad (3)$$

in which N=4 is the peak amount of TiN, I_{hkl} and $I_{0,hkl}$ are the integrated intensity of the (hkl) Bragg reflection for the studied and for a randomly oriented samples, respectively, as give in ICDD: 00-038-1420. In the present study, 4 main diffraction peaks (111), (200), (220) and (420) are taken into account. The percentage of texture coefficient T_{c_hkl} % is defined as T_{c_hkl} /N to show the preferred orientation of TiN films in the present work.

Figure 6 presents the relationship between the preferred orientation of TiN, growth rate, supersaturation, and deposition temperature on various substrates. In CVD, high deposition temperatures are generally correlated to low supersaturations. In Figure 6a, the substrates are stainless steel, WC-Co or graphite which are only poorly or randomly textured. It can be seen that the orientation of TiN is correlated with supersaturation. TiN film with (111) preferred orientation appears at low supersaturation (high temperature) while (200) and (220) preferred orientation are likely grown at high supersaturation (so low temperature), in agreement with Ref. [35]. In Figure 6b, the substrates are (0001) single crystal sapphire. Due to crystallographic relationships, the (0001) hexagonal lattice of sapphire imposes the (111) preferred orientation to the TiN film. High supersaturation (Log_{10} (supersaturation) >15.5) contributes to polycrystalline TiN film. It also can be seen from Figure 7 that there is no clear correlation between N/Ti ratio and the crystallographic orientation of TiN films.

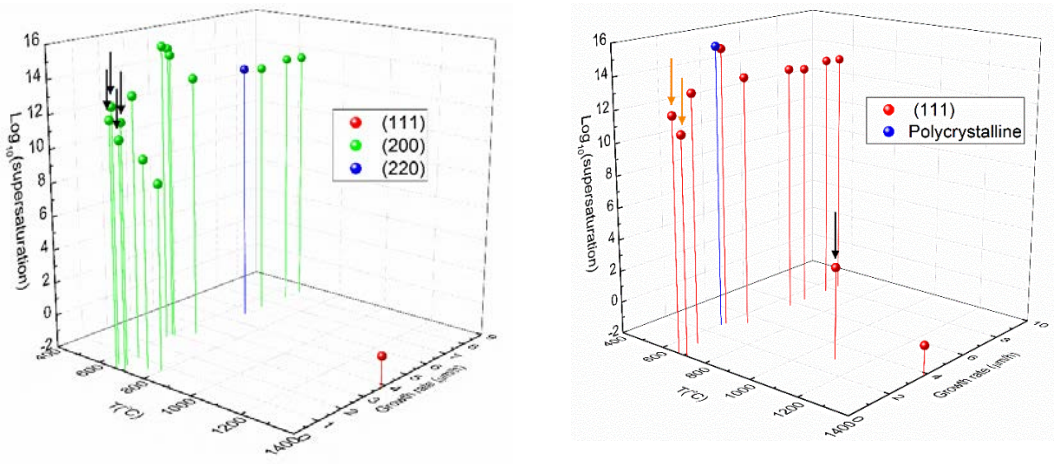

(a) **(b)**

Figure 6. Relationships among preferred orientations, growth rates, supersaturation and deposition temperatures. (a) Substrates are WC-Co, stainless steel and graphite without preferred orientation. (b) Substrate is (0001) sapphire. Black arrows show TiN films with golden color and orange arrows show TiN films with silver color.

4.3. The formation conditions and feature of golden TiN

Even if the color of TiN film is affected by various properties such as composition, stoichiometry and thickness etc. [36], we studied color feature as function of process parameters (N/Ti gas phase ratio, supersaturation) and finally cross-section morphology. In Figure 6, the black and orange arrows point out the conditions for obtaining golden TiN films and silvery TiN films, respectively. On non-oriented substrates, golden color is obtained at rather low growth rate (less than 0.4 μm/h). On (0001) sapphire, silver and golden TiN films prefer low growth rate (less than 3 μm/h). TiN films with both (200) and (111) preferred orientation can have golden color. Polycrystalline TiN with golden color can also be obtained (see Figure S2 in supplementary material). Therefore, the golden color of TiN is clearly not related with its texture.

In Ref. [37], the color of TiN films was studied in a small range of growth rates, less than 2 μm/h. It showed that the color of TiN films was determined by N/Ti gas-phase ratio. In our experiments, the range of growth rate is from 0.03 to 8 μm/h at various N/Ti ratios on single and polycrystalline substrates. So it is interesting to study TiN color according to these two parameters only. Figure 7 presents the influence of N/Ti on growth rate and color of TiN on non-orientated substrates (Figure 7a) and (0001) sapphire single crystal (Figure 7b). It can be seen that high N/Ti ratio leads to high growth rate. Figure 7a shows that on polycrystalline substrates, the color of TiN is mainly influenced by growth rate. The golden TiN can be obtained when the growth rate is below 0.4 μm/h. Figure 7b shows that the influence of N/Ti ratio and growth rate on the color of TiN films grown on (0001) sapphire single crystal is more complicated. The sapphire substrates have an ordered structure and transparent color. Golden color is difficult to obtain because TiN film with (111) crystallographic orientation prefers to grow as columnar layer, not dense enough. When the growth rate is less than 0.1 μm/h, TiN films present a silvery color. The color of TiN films changes from silver to golden with deposition time (visual observation during experiments). When the N/Ti ratio is around 2 and growth rate is around 3 μm/h, TiN film with shining golden color is obtained once. The brown TiN films are obtained when the growth rate is above 3 μm/h or N/Ti ratio is above 2. In conclusion, golden TiN films on non-orientated substrates are determined by a low growth rate (≤0.4 μm/h) while on sapphire film should be thick enough (≈ 3 μm) and not columnar (dense).

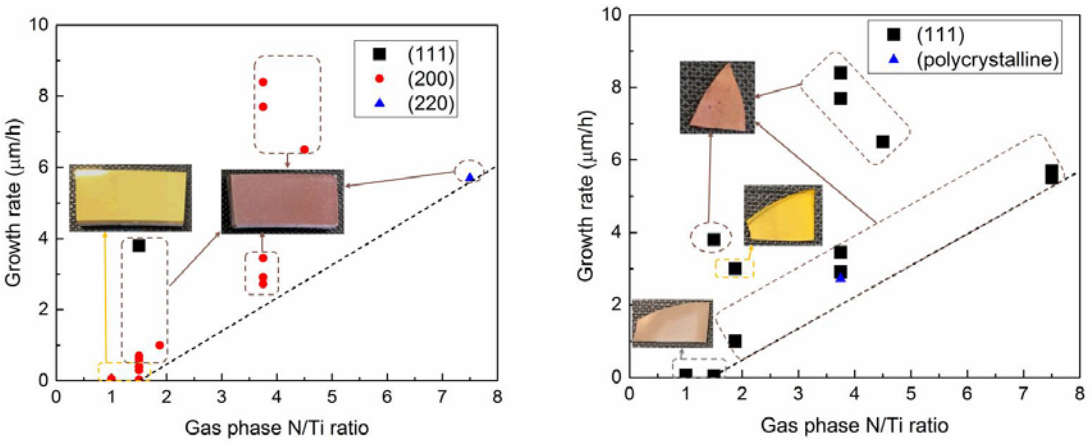

Figure 7. TiN growth rate versus N/Ti ratio on (a) non-orientated substrates and (b) (0001) sapphire. The figure also indicates the preferred orientation and color of TiN.

To show the structure difference between golden and brown TiN, Figure 8 shows cross-sectional morphology of (a) golden TiN on WC-Co, (b) brown TiN on WC-Co. On non-orientated substrates, it can be see that thin and dense TiN layers present golden color while TiN films with thick columnar structure present brown color.

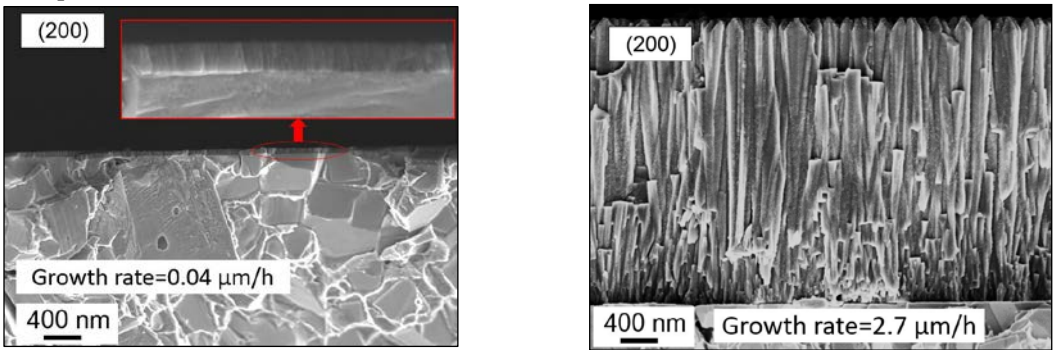

Figure 8. Cross-sectional morphology of (a) golden TiN on WC-Co (b) brown TiN on WC-Co. The figure also indicates preferred crystallographic direction and growth rate.

Three cross-sectional and surface morphology of TiN films: (a) golden, growth rate at 3 μm/h, N/Ti=1.875, (b) brown, growth rate at 3 μm/h, N/Ti=3.75 and (c) brown, growth rate at 5.7 μm/h, N/Ti=7.5 on sapphire are shown in Figure 9. Morphology in Figure 9(a) shows very dense TiN film while there are gaps between columns in Figure 9(b) and (c). Especially (a) and (b) has the same growth rate and thickness, it indicates that dense structure is the key point for the golden TiN film. Increasing N/Ti ratio as shown in Figure 9(b) or increasing both N/Ti ratio and growth rate as shown in Figure 9(c) leads to columnar growth and present brown color. As a conclusion, dense TiN films are always golden. Low N/Ti ratio leads to high density.

(a)

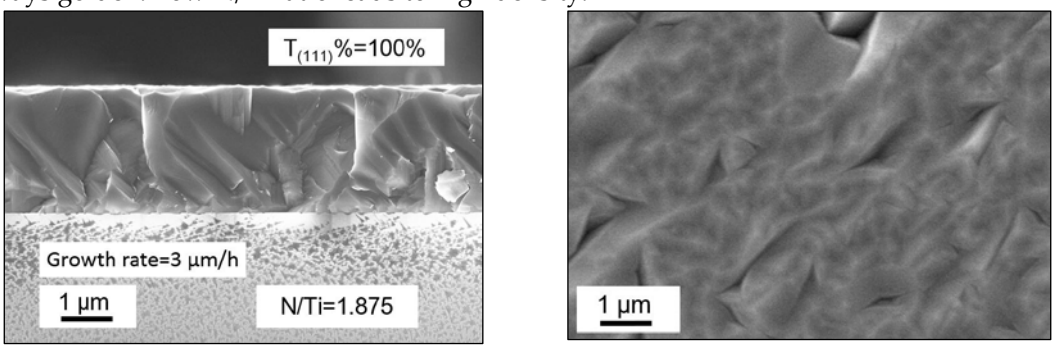

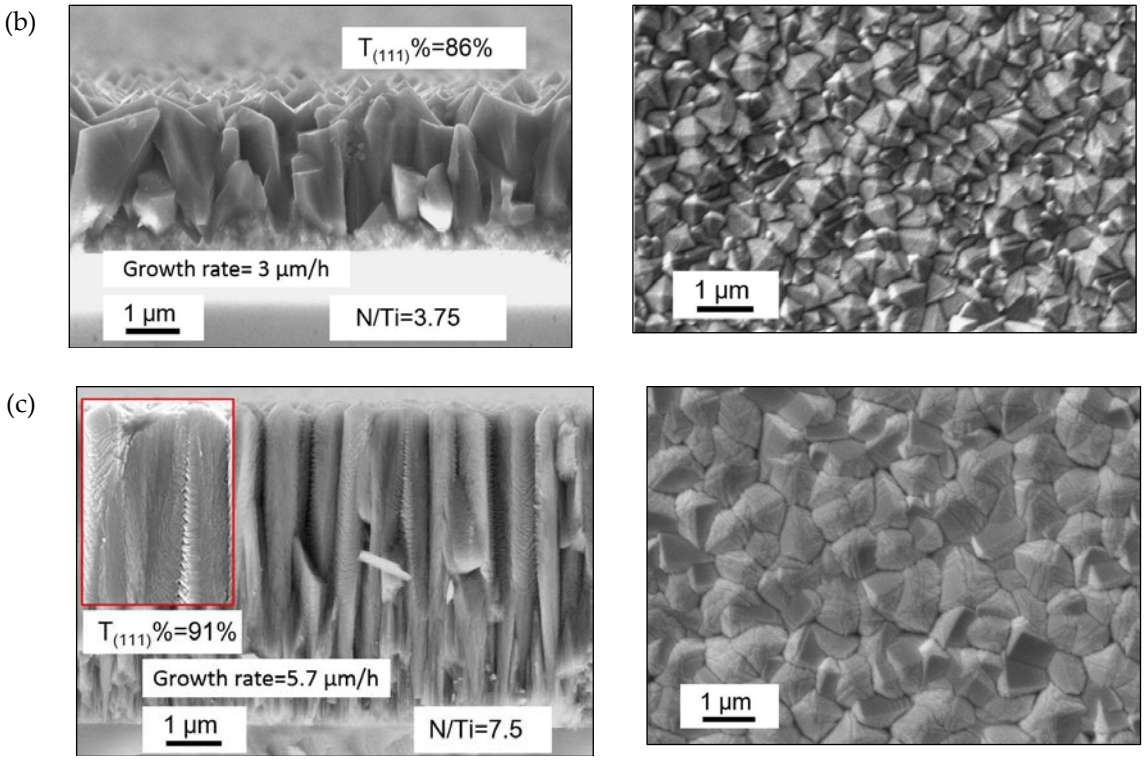

Figure 9. Cross-sectional and surface morphology for TiN layers with (a) golden (b) brown (c) brown color on sapphire. The figure also indicates preferred crystallographic orientation, growth rate and N/Ti ratio.

5. Conclusions

A simplified kinetic model associated with heat and mass transport for TiN film growth was proposed. $TiCl_3$ and $TiCl_4$ are the most important Ti-containing gas-phase species. These species are adsorbed on the growing surface with an activation energy close to 43 kJ/mol. The model has been validated within a broad range of process parameters (temperature, N/Tigas-phase ratio, pressure).

The relationship between growth rate, supersaturation, deposition temperature and preferred orientation was studied. It was shown that the orientation of TiN films on non-orientated substrates is influenced by both supersaturation and deposition temperature. TiN films with (111) dominated orientation are preferably grown at low supersaturation and high temperature while (200) and (220) preferred orientation at high supersaturation and low temperature. On (0001) sapphire single crystal, TiN thin films with (111) preferred orientation are most likely to be growing. There is no obvious relationship between the golden color and texture.

Golden TiN films were obtained when the growth rate is lower than 0.4 µm/h. Otherwise, TiN films are brown because of columnar structure. On (0001) sapphire single crystals, TiN films should be thick (≈ 3 µm) and dense enough to obtain a golden color. The main characteristic of golden TiN films is found to be a dense structure, whatever the process parameters used to get this property.

Supplementary Materials: Table S1: Governing equations of multicomponent mass and heat transfer. Table S2: The gas phase reactions and rate constant for reaction K is represented in the standard Arrhenius form. Table S3: Surface reactions and correspond kinetic parameters used in the simplified model. Figure S1: Purple $TiCl_3$ films on the quartz tube. Figure S2: The surface morphology of polycrystalline TiN with golden color on WC-Co.

Author Contributions: Conceptualization, Michel Pons, Frederic Mercier and Raphaël Boichot; Experiments, Juan Su; Simulation, Juan Su, Michel Pons, Elisabeth Blanquet and Raphaël Boichot. Writing-Original Draft Preparation, Juan Su.; Writing-Review & Editing, Michel Pons, Frederic Mercier, Elisabeth Blanquet and Raphaël Boichot; Project Administration, Raphaël Boichot.

Funding: This research was supported by Carnot Institute 'Énergies du Futur' for the project "AlN pour materiaux refractaires fonctionnels' and by the Centre of Excellence of Multifunctional Architectured Materials "CEMAM" [grant number ANR-10-LABX-44-01].

Acknowledgments: The authors want to thank R. Reboud for emergency management during experiments, M. Jaquemin for help in experiments, S. Coindeau and T. Encinas for discussions on the XRD results.

References

1. Echigoya, J.; Liu, Z.-t.; Imamura, A.; Takatsu, S. Transmission electron microscopy studies of growth and interface structure of chemically vapour deposited TiC and TiN films on WC-Co alloy substrates. *Thin Solid Films* **1991**, *198*, 293-300, doi:10.1016/0040-6090(91)90347-Z.
2. Prengel, H.G.; Pfouts, W.R.; Santhanam, A.T. State of the art in hard coatings for carbide cutting tools. *Surface and Coatings Technology* **1998**, *102*, 183-190, doi:10.1016/S0257-8972(96)03061-7.
3. Matei, A.A.; Pencea, I.; Branzei, M.; Tranca, D.E.; Tepes, G.; Sfatb, C.E.; Ciovica, E.; Gherghilescu, A.I.; Stanciu, G.A. Corrosion resistance appraisal of TiN, TiCN and TiAlN coatings deposited by CAE-PVD method on WC-Co cutting tools exposed to artificial sea water. *Applied Surface Science* **2015**, *358*, 572-578, doi:10.1016/j.apsusc.2015.08.041.
4. Rebenne, H.E.; Bhat, D.G. Review of CVD TiN coatings for wear-resistant applications: deposition processes, properties and performance. *Surface and Coating Technology* **1994**, *63*, 1-13, doi:10.1016/S0257-8972(05)80002-7.
5. Wagner, J.; Mitterer, C.; Penoy, M.; Michotte, C.; Wallgram, W.; Kathrein, M. The effect of deposition temperature on microstructure and properties of thermal CVD TiN coatings. *International Journal of Refractory Metals and Hard Materials* **2008**, *26*, 120-126, doi:10.1016/j.ijrmhm.2007.01.010.
6. Kashani, H.; Sohi, M.H.; Kaypour, H. Microstructural and physical properties of titanium nitride coatings produced by CVD process. *Materials Science and Engineering A* **2000**, *286*, 324-330, doi:10.1016/S0921-5093(00)00744-9.
7. Fiordalice, R.W.; Hegde, R.I.; Kawasaki, H. Orientation control of chemical papor deposition TiN film for barrier applications. *Journal of the Electrochemical Society* **1996**, *143*, doi:10.1149/1.1836949.
8. DelaCruz, S.; Wang, Z.; Cheng, P.; Carraro, C.; Maboudian, R. TiN diffusion barrier for stable W/SiC(0001) interfaces in inert ambient at high temperature. *Thin Solid Films* **2019**, *670*, 54-59, doi:10.1016/j.tsf.2018.11.058.
9. Sato, M.; Takeyama, M.B. Relationship between TiN films with different orientations and their barrier properties. *Japanese Journal of Applied Physics* **2018**, *57*, 07MB01-07MB03, doi:10.7567/JJAP.57.07MB01.
10. Grosso, S.; Latu-Romain, L.; Berthome, G.; Renou, G.; Coz, T.L.; Mantel, M. Titanium and titanium nitride thin films grown by dc reactive magnetron sputtering Physical Vapor Deposition in a continuous mode on stainless steel wires: Chemical, morphological and structural investigations. *Surface and Coatings Technology* **2017**, *324*, 318-327, doi:10.1016/j.surfcoat.2017.05.089.
11. Roquiny, P.; Bodart., F.; Terwagne, G. Colour control of titanium nitride coatings produced by reactive magnetron sputtering at temperature less than 100°C. *Surface and Coatings Technology* **1999**, *116-119*, 278-283, doi:10.1016/s0257-8972(99)00076-6.
12. Kafizas, A.; Carmalt, C.J.; Parkin, I.P. CVD and precursor chemistry of transition metal nitrides. *Coordination Chemistry Reviews* **2013**, *257*, 2073-2119, doi:10.1016/j.ccr.2012.12.004.
13. Choy, K.L. Chemical vapour deposition of coatings. *Progress in Materials Science* **2003**, *48*, 57-170, doi:10.1016/S0079-6425(01)00009-3.

14. García, J.; Pinto, H.; Ramos-Moore, E.; Espinoza, C.; Östby, J.; Coelho, R. In-situ high temperature stress analysis of Ti(C,N) coating on functionally graded cemented carbides by energy dispersive synchrotron X-ray diffraction. *International Journal of Refractory Metals and Hard Materials* **2016**, *56*, 27-34, doi:10.1016/j.ijrmhm.2015.12.001.
15. Tang, S.; Gao, S.; Wang, S.; Wang, J.; Zhu, Q.; Chen, Y.; Li, X. Characterization of CVD TiN coating at different deposition temperatures and its application in hydrocarbon pyrolysis. *Surface and Coatings Technology* **2014**, *258*, 1060-1067, doi:10.1016/j.surfcoat.2014.07.029.
16. von Fieandt, L.; Larsson, T.; Lindahl, E.; Bäcke, O.; Boman, M. Chemical vapor deposition of TiN on transition metal substrates. *Surface and Coatings Technology* **2018**, *334*, 373-383, doi:10.1016/j.surfcoat.2017.11.063.
17. Dekker, J.P.; Put, P.J.v.d.; Veringa, H.J.; Schoonman, J. A kinetic study of titanium nitride chemical vapor deposition using Nitrogen, Hydrogen, and Titanium Tetrachloride. *Journal of The Electrochemical Society* **1994**, *141*, 787-795, doi:10.1149/1.2054812
18. Spee, C.I.M.A.; Driessen, J.P.A.M.; Kuypers, A.D. Low temperature deposition of TiN ceramic material by metal organic and/or plasma enhanced CVD. *Le Journal de Physique IV* **1995**, *05*, C5-719-C715-734, doi:10.1051/jphyscol:1995587.
19. Kuo, D.-H.; Huang, K.-W. Kinetics and microstructure of TiN coatings by CVD. *Surface and Coatings Technology* **2001**, *135*, 150-157, doi:10.1016/S0257-8972(00)00986-5.
20. Jiang, C.; Goto, T.; Hirai, T. Morphology and preferred orientation of titanium nitride plates prepared by chemical vapour deposition. *Journal of Materials Science* **1994**, *29*, 669-675, doi:10.1007/BF00445977.
21. Nakanishi, N.; Mori, S.; Kato, E. Kinetics of chemical vapor deposition of titanium nitride. *Journal of The Electrochemical Society* **1990**, *137*, 322-328, doi:10.1149/1.2086412.
22. Larson, R.S.; Allendorf, M.D. *A reaction mechanism for titanium nitride CVD from $TiCl_4$ and NH_3*; SAND96-8443·UC-401, Sandia National Laboratories: California, May 5-10, 1996, 1996; pp 41-46.
23. Allendorf, M.D.; Arsenlis, A.; Bastasz, R.; Colvin, M.E.; Evans, G.; Germann, G.; Janssen, C.L.; Larson, R.S.; Melius, C.F.; Osterheld, T.H., et al. *Development of a Process Simulation Capability for the Formation of Titanium Nitride Diffusion barriers*; SAND97-8235·UC-404, Sandia National Laboratories: California, 1997; pp 1-40.
24. Grujicic, M.; Lai, S.G. Multi-length scale modeling of chemical vapor deposition of titanium nitride coatings. *Journal of Materials Science* **2001**, *36*, 2937-2953, doi:10.1023/A:1017958621586.
25. Teyssandier, F.; Allendorf, M.D. Thermodynamics and kinetics of gas-phase reactions in the Ti-Cl-H system. *Journal of the Electrochemical Society* **1998**, *145*, 2167-2177, doi:10.1149/1.1838613.
26. J.Herzler; Roth, P. High-temperature decomposition of $TiCl_4$ based on Cl-Concentration measurements. *Proceedings of the Combustion Institute* **2002**, *29*, 1353-1359, doi:10.1016/S1540-7489(02)80166-3.
27. Umanskii, S.Y.; Novoselov, K.P.; Minushev, A.K.; Siodmiak, M.; Frenking, G.; Korkin, A.A. Thermodynamics and kinetics of initial gas phase reactions in chemical vapor deposition of titanium nitride. Theroretical study of TiCl4 Ammonolysis. *Journal of Computational Chemistry* **2001**, *22*, 1366, doi:10.1002/jcc.1095.
28. Boichot, R.; Coudurier, N.; Mercier, F.; Claudel, A.; Baccar, N.; Milet, A.; Blanquet, E.; Pons, M. CFD modeling of the high-temperature HVPE growth of aluminum nitride layers on c-plane sapphire: from theoretical chemistry to process evaluation. *Theoretical Chemistry Accounts* **2014**, *133*, doi:10.1007/s00214-013-1419-8.
29. Bird, R.B.; Stewart, W.E.; lightfoot, E.N. *Transport phenomena, Rivesed 2nd ed.*; Wiley, J., New York, 2002.
30. Svehla, R.A. *NASA technical report R-132.* ; 1962.
31. Chase, M.W. *JANAF Thermochemical tables, 4th ed.*; American Chemical Society ; Woodbury, N.Y. : American Institute of Physics for the National Institute of Standards and Technology: Washington, D.C., 1998.

32. Mercier, F.; Shimoda, H.; Lay, S.; Pons, M.; Blanquet, E. Reactive chemical vapor deposition of heteroepitaxial Ti1−xAlxN films. *CrystEngComm* **2018**, *20*, 1711-1715, doi:10.1039/c7ce02129a.
33. Kurtz, S.R.; Gordon, R.G. Chemical vapor deposition of titanium nitride at low temperatures. *Thin Solid Films* **1986**, *140*, 277-290, doi:10.1016/0040-6090(86)90271-3.
34. Consonni, V.; Rey, G.; Roussel, H.; Bellet, D. Thickness effects on the texture development of fluorine-doped SnO2 thin films: The role of surface and strain energy. *Journal of Applied Physics* **2012**, *111*, 033523, doi:10.1063/1.3684543.
35. Pangarov, N.A. On the crystal orientation of electrodeposited metals. *Electrochimica Acta* **1964**, *9*, 721-726, doi:10.1016/0013-4686(64)80060-8.
36. Anderbouhr, S.; Blanquet, E.; Ghetta, V.; Bernard, C. TiN and $(Ti_{1-x}Al_x)N$ films obtained by a low pressure chemical vapor deposition process. In Proceedings of Proc 14th Int conf chem vap dep and EUROCVD XI, Pennington, 1997; pp. 356-363.
37. Nah, J.-W.; Kim, B.-J.; Lee, D.-K.; Lee, J.-J. Color, structure, and properties of TiN coatings prepared by plasma enhanced chemical vapor deposition. *Journal of Vacuum Science & Technology A* **1999**, *17*, 463-469, doi:10.1116/1.581607.

Supplementary materials

Chemical vapor deposition of titanium nitride thin films: kinetics and experiments

Juan Su [1], Raphaël Boichot [1,*], Elisabeth Blanquet [1], Frédéric Mercier [1], and Michel Pons [1]

Heat and Mass transport model

The governing equations describing flow dynamics, heat and mass transfer are shown in Table S1. Precursors are very diluted in H_2 (more than 90% in mole fraction of the gaseous phase), so values of the transport properties can be calculated by the kinetic theory of dilute gas[1].

The boundary conditions for heat transfer are: $T = T_m$ on the surface of substrate and $T = T_c$ on the cooling wall (T_m is measured from IR pyrometer and T_c is controlled by a heating and cooling system); the temperature for initial gas-phase species are room temperature. The boundary conditions for mass transfer are: the velocity on the wall is 0; the velocity at the inlet is varied to satisfy the calculated flow rates matching the experimental conditions. Outlet condition is zero pressure (compared to the reference working pressure).

Table S1. Governing equations of multicomponent mass and heat transfer (notations are at the end of the document).

Continuity	$\nabla \cdot \rho\vec{v} = 0$
Momentum balance (1)	$\nabla \cdot \left(\rho\vec{v}\vec{v}\right) = \nabla \cdot \underline{\underline{\tau}} - P + \rho\vec{g}$ $\underline{\underline{\tau}} = \mu\left(\nabla\vec{v} + (\nabla\vec{v})^t\right) - \frac{2}{3}\mu(\nabla \cdot \vec{v}) \cdot \underline{\underline{I}}$
Energy balance (2)	$c_p \nabla \cdot \left(\rho\vec{v}T\right) = \nabla \cdot \left(\lambda\nabla T\right) + \nabla \cdot \left(RT\sum_{i=1}^{N} \frac{D_i^T}{M_i}\frac{\nabla x_i}{x_i} \right)$ $+\sum_{i=1}^{N} \frac{H_i}{M_i}\nabla \cdot \vec{J}_i - \sum_{i=1}^{N}\sum_{k=1}^{K} H_i \upsilon_{ik}\left(\mathcal{R}_k^g - \mathcal{R}_{-k}^g\right)$
Species transport (3)	$\nabla \cdot \left(\rho\vec{v}\omega_i\right) = -\nabla \cdot \vec{J}_i + M_i\sum_{k=1}^{K}\upsilon_{ik}\left(\mathcal{R}_k^g - \mathcal{R}_{-k}^g\right)\ i = 1, N$ $\vec{J}_i^c = -\sum_{j=1}^{N}\left(\rho D_{ij}\right)\nabla x_j\ \ i = 1, N$ $\vec{J}_i^T = -D_i^T\frac{\nabla T}{T}\ i = 1, N$
Ideal gas law (4)	$\rho = \frac{PM}{RT}$
Deposition rate (5)	$R_s = \vec{J}_i.\vec{n} = \vec{J}_i^c.\vec{n} + \vec{J}_i^T.\vec{n}\ i = 1, N$

Gas-phase kinetics pathways

From thermodynamic equilibrium calculation in chlorination tube, both $TiCl_4$ and $TiCl_3$ should be considered for the gas-phase reactions. The gas-phase kinetic model involves unimolecular

dissociation reactions (K1-K3) and bimolecular reactions (K4-K17) is summarized in Ref[1] (Table S2). The rate constant for reaction k_k in this work is represented in the standard Arrhenius form:

$$k_k = \alpha_k T^{\beta_k} \exp\left(-\frac{E_{\alpha k}}{RT}\right) \quad \text{(S1)}$$

Table S2. The rate constant for reaction K is represented in the standard Arrhenius form: $k_k = \alpha_k T^{\beta_k} \exp\left(-\frac{E_{\alpha k}}{RT}\right)$. For unimolecular reactions, the units of α_k are s^{-1}; for bimolecular reactions, the units are $cm^3\ mol^{-1}\ s^{-1}$. All energies are in kJ mol^{-1}.

Reaction K	α_k	β_k	$E_{\alpha k}$
K1: $TiCl_4$ <-> $TiCl_3$ + Cl	2.32 E+20	-1.17	387.9
K2: $TiCl_3$ <-> $TiCl_2$ + Cl	1.02E+18	-0.742	422.6
K3: $TiCl_2$ <-> TiCl + Cl	3.65E+20	-1.06	509.6
K4: $TiCl_4$ + H <-> $TiCl_3$ + HCl	5.11E+06	2.5	12.6
K5: $TiCl_3$ + H <-> $TiCl_2$ + HCl	1.11E+06	2.5	33.5
K6: $TiCl_2$ + H <-> TiCl + HCl	3.05E+06	2.5	145.2
K7: TiCl +H <-> Ti + HCl	4.09E+05	2.5	24.7
K8: H+Cl+M -> HCl + M	7.20E+21	-2.0	0.0
K9: HCl + M -> HCl + M	7.90E+25	-3.0	445.6
K10: Cl + Cl + M <-> Cl_2 + M	2.00E+14	0.0	-7.5
K11: H + HCl -> Cl + H_2	1.69E+13	0.0	17.2
K12: Cl + H_2 -> H + HCl	2.95E+13	0.0	21.3
K13: Cl_2 + H <-> Cl + HCl	8.60E+13	0.0	5.0
K14: H + H + H_2 -> H_2 + H_2	9.70E+16	-0.6	0.0
K15: H_2 + H_2 -> H + H + M	8.80E+14	0.0	402.1
K16: H_2 + M -> H + H + M	2.20E+14	0.0	402.1
K 17: H + H + M -> H_2 + M	6.53E+17	-1.0	0.0

Surface kinetics pathways

The surface reaction rate for adsorbed species *C_s* which absorb the gas-phase molecules A is expressed as [2]:

$$V_k = k_k[A] \times [C(S)] \tag{S2}$$

The rate constant for reaction k_k in this work is represented in the standard Arrhenius form:

$$k_k = \alpha_k T^{\beta_k} \exp\left(-\frac{E_{\alpha k}}{RT}\right) \tag{S3}$$

In which,

$$\alpha_k = \sqrt{\frac{R}{2\pi M_A}} \frac{1}{[\Gamma_{tot}]} \tag{S4}$$

$$\beta_k = 0.5 \tag{S5}$$

The local gas supersaturation near the growing surface has been defined as the sum of the reactants pressure divided by the sum of the species at equilibrium pressure [3]:

$$\beta = \frac{P_{\mathrm{TiCl_3}} + P_{\mathrm{TiCl_4}} + P_{\mathrm{NH_3}}}{P^*_{\mathrm{Ti}} + 2P^*_{\mathrm{N_2}}} \tag{S6}$$

where P and P^* are calculated pressure of species ($TiCl_3$, $TiCl_4$, and NH_3) contributing to TiN growth near the growing surface and the equilibrium vapor pressure of gases in a closed volume at the same temperature calculated with Factsage 7.1.

Table S3. Surface reactions and correspond kinetic parameters used in the simplified model. _s is a surface site and (*B*) is the bulk phase. The surface density is 1.8×10^{-9} mol cm^{-2}.

Heterogeneous reaction unit CGS (cm-g-s)			
Surface reactions	$\boldsymbol{\alpha_k}$ **Pre exp. factor**	$\boldsymbol{\beta_k}$ **Temp. exp.**	$\boldsymbol{E_{\alpha k}/R}$ **Activ. temp. (K)**
$\mathrm{TiCl_3} + \mathrm{NH_2}\_s \leftrightarrow \mathrm{N}(B) + \mathrm{TiCl_2}\_s + \mathrm{HCl}$	1E+14	0.5	4900
$\mathrm{TiCl_4} + \mathrm{NH_2}(S) \rightarrow \mathrm{N(B)} + \mathrm{TiCl_3}(S) + \mathrm{HCl}$	1E+14	0.5	4900
$\mathrm{NH_3} + \mathrm{TiCl_2}\_s \rightarrow \mathrm{Ti}(B) + \mathrm{NH_2}\_s + \mathrm{HCl} + \mathrm{Cl}$	2.4E+11	0.5	4900
$\mathrm{NH_3} + \mathrm{TiCl_3}(S) \rightarrow \mathrm{Ti}(B) + \mathrm{NH_2}(S) + \mathrm{HCl} + \mathrm{Cl_2}$	2.4E+11	0.5	4900

Supplementary results

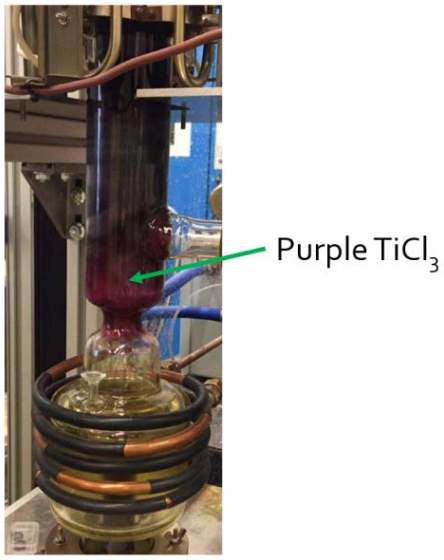

Figure S1. Purple $TiCl_3$ films on the quartz tube.

Figure S1 shows the purple powdered films deposited on the quartz after experiments. In fact, the color of the quartz varied from light purple, dark purple to black with deposition time because the thickness increase.

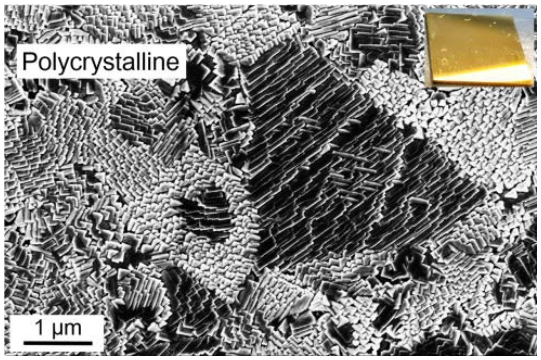

Figure S2. Polycrystalline TiN with golden color on WC-Co obtained from another CVD system in our lab.

References for the supporting information

1. Teyssandier, F.; Allendorf, M.D. Thermodynamics and kinetics of gas-phase reactions in the Ti-Cl-H system. *Journal of the Electrochemical Society* **1998**, *145*, 2167-2177, doi:10.1149/1.1838613.
2. Coltrin, M.E.; Kee, R.J.; Rupley, F.M.; Meeks, E. *Surface chemkin*; SAND96-8217·UC-405, Sandia National Laboratories: Livermore, California, 1990.
3. Boichot, R.; Coudurier, N.; Mercier, F.; Claudel, A.; Baccar, N.; Milet, A.; Blanquet, E.; Pons, M. CFD modeling of the high-temperature HVPE growth of aluminum nitride layers on c-plane sapphire: from theoretical chemistry to process evaluation. *Theoretical Chemistry Accounts* **2014**, *133*, doi:10.1007/s00214-013-1419-8.

Notations and units

R_S	:	surface reaction rate ($kg.m^{-2}.s^{-1}$)
$\underline{v}$	:	velocity vector ($m.s^{-1}$)
P	:	pressure (Pa)
x_i	:	species molar fraction of species i

ω_i	:	species mass fraction of species i
T	:	temperature (K)
g	:	gravity vector (g = 9.81 m.s^{-2})
I	:	unity tensor
R	:	universal gas constant (8.314 J.mol^{-1}.K^{-1})
M	:	molar mass of the mixture (kg.mol^{-1})
N	:	number of gaseous species in the mixture
ρ	:	density (kg.m^{-3})
λ	:	thermal conductivity of the gas mixture (W.m^{-1}.K^{-1})
μ	:	dynamic viscosity of the gas mixture (kg.m^{-1}.s^{-1})
C_p	:	specific heat of the gas mixture (J.kg^{-1}.K^{-1})
$\underline{n}$	:	unity vector normal
ρ	:	density (kg.m-3)
h	:	advection coefficient (W.m^{-2}.K^{-1})
T_{amb}	:	ambient temperature (K)
σ_{st}	:	Stefan-Boltzmann constant (W.m^{-1}.K^{-4})
ε	:	emissivity
n	:	unity vector normal to the wall
$\Re_{gi}$	:	reaction rate of reaction i in the gas phase (kg.m^{-3}.s^{-1})
$\mathbf{J}_i^F$	:	diffusive mass flux vector (kg.m^{-2}.s^{-1})
$\mathbf{J}_i^T$	:	thermo-diffusive mass flux vector (kg.m^{-2}.s^{-1})
D_{ij}	:	multicomponent diffusion coefficients (m^{-2}.s^{-1})
D_i^T	:	multicomponent thermodiffusion coefficients (kg. m^{-1}.s^{-1})
Γ_{tot}	:	total surface site concentration (mol m^{-2})
M_A	:	Molar mass for gaseous specie *A* (kg mol^{-1})
$E_{\alpha k}$	:	activation energy for reaction *k* (J mol^{-1})
V_k	:	production rate of solid surface for reaction *k* (mol m^{-2} s^{-1})